HHS Public Access

Author manuscript

Cell Rep. Author manuscript; available in PMC 2021 October 08.

Published in final edited form as:

Cell Rep. 2021 August 24; 36(8): 109580. doi:10.1016/j.celrep.2021.109580.

Fusion pores with low conductance are cation selective

Joannalyn B. Delacruz[1], **Satyan Sharma**[2,3], **Shailendra Singh Rathore**[1], **Meng Huang**[1], **Joan S. Lenz**[1], **Manfred Lindau**[1,2,4,*]

[1]School of Applied & Engineering Physics, Cornell University, 142 Sciences Drive, Ithaca, NY 14853, USA

[2]Nanoscale Cell Biology Group, Max-Planck-Institute for Biophysical Chemistry, Am Fassberg 11, 37077 Göttingen, Germany

[3]Medical Informatics in Translational Oncology, German Cancer Research Center (DKFZ), Im Neuenheimer Feld 280, 69120 Heidelberg, Germany

[4]Lead contact

SUMMARY

Many neurotransmitters are organic ions that carry a net charge, and their release from secretory vesicles is therefore an electrodiffusion process. The selectivity of early exocytotic fusion pores is investigated by combining electrodiffusion theory, measurements of amperometric foot signals from chromaffin cells with anion substitution, and molecular dynamics simulation. The results reveal that very narrow fusion pores are cation selective, but more dilated fusion pores become anion permeable. The transition occurs around a fusion pore conductance of ~300 pS. The cation selectivity of a narrow fusion pore accelerates the release of positively charged transmitters such as dopamine, noradrenaline, adrenaline, serotonin, and acetylcholine, while glutamate release may require a more dilated fusion pore.

Graphical Abstract

*Correspondence: ML95@cornell.edu.

AUTHOR CONTRIBUTIONS

J.B.D., S.S.R., M.H., and M.L. performed experiments and data analysis. J.B.D., S.S.R., and J.S.L. performed cell preparations. S.S. performed the computational simulations. J.B.D., S.S., S.S.R., and M.L. designed experiments and wrote the paper.

INCLUSION AND DIVERSITY

One or more of the authors of this paper self-identifies as an underrepresented ethnic minority in science. One or more of the authors of this paper received support from a program designed to increase minority representation in science. While citing references scientifically relevant for this work, we also actively worked to promote gender balance in our reference list. The author list of this paper includes contributors from the location where the research was conducted who participated in the data collection, design, analysis, and/or interpretation of the work.

DECLARATION OF INTERESTS

The authors declare no competing interests.

SUPPLEMENTAL INFORMATION

Supplemental information can be found online at https://doi.org/10.1016/j.celrep.2021.109580.

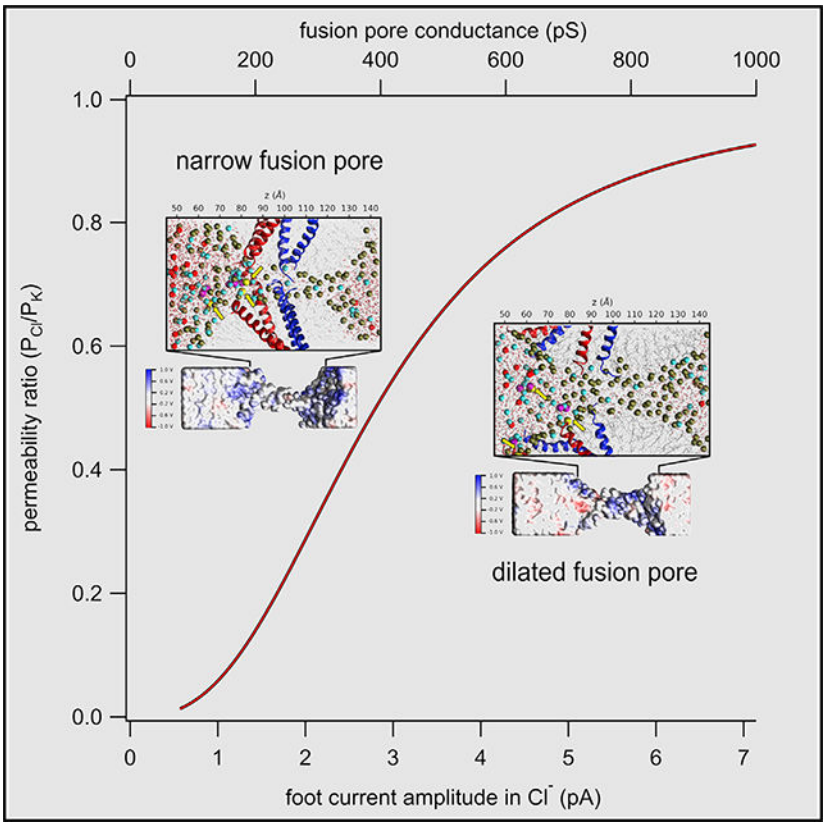

In brief

For transmission, a fusion pore forms when vesicle and target membranes are brought together by SNARE proteins. Delacruz et al. demonstrate that selectivity of the pore accelerates release of positively charged transmitters such as dopamine, noradrenaline, adrenaline, serotonin, and acetylcholine, while glutamate release may require a more dilated fusion pore.

INTRODUCTION

Release of hormones and neurotransmitters occurs by exocytosis, which is initiated by the formation of a narrow fusion pore (Breckenridge and Almers, 1987; Sharma and Lindau, 2018a). Although some fusion pores expand very rapidly, others remain stable as a fusion pore of molecular dimensions, with a diameter of ~1–2 nm and a lifetime on the millisecond timescale (Chow et al., 1992; Zhao et al., 2013; Shin et al., 2018). Understanding how transmitter molecules permeate the early fusion pore is essential for a mechanistic understanding of fast transmitter release in the nervous system. Many fast-acting neurotransmitters, such as acetylcholine and glutamate, carry a net charge, which requires charge compensation when they are released through the fusion pore. Therefore, transmitter release through the fusion pore is a process of electrodiffusion (Gong et al., 2007).

The flux of the positively charged catecholamine molecules from single vesicles can be measured in chromaffin cells by a carbon fiber microelectrode (CFM) as an amperometric

current spike that results from the oxidation (not the cationic net charge) of the released molecules (Wightman et al., 1991). Such amperometric spikes are frequently preceded by a so-called foot signal (Chow et al., 1992) that reflects the flux of catecholamines through the fusion pore (Albillos et al., 1997).

Previous experiments have shown that in chromaffin cells early fusion pores have variable conductance with a mean value of ~330 pS and that catecholamines permeate the fusion pore at a rate that fluctuates proportional to its conductance (Albillos et al., 1997; Gong et al., 2007). Although most of the vesicular catecholamines are bound to the vesicular matrix, there is a fraction of free catecholamines at ~200–300 mM concentration that is readily available for release through the fusion pore. Reducing the extracellular NaCl concentration decreases the magnitude of foot currents, indicating that positive charge carried by catecholamines out of the vesicle is compensated by influx of Na^+ ions into the vesicle through the fusion pore and that there is no significant co-release of anions (Gong et al., 2007). Chromaffin granules contain a high concentration of ATP, as the main negatively charged ion. It is unknown if the apparent lack of ATP co-release through the fusion pore is due to cation selectivity of the fusion pore or ATP's being unavailable for release via the fusion pore because it is bound to the granular matrix (Pollard et al., 1979) or in a complex with bound catecholamines (Kopell and Westhead, 1982; Estévez-Herrera et al., 2016). Cation selectivity of the fusion pore might be expected if the fusion pore is lined by negative charges from lipids and/or proteins.

Acetylcholine, serotonin, and catecholamines carry a positive charge and would permeate a cation-selective fusion pore. However, glutamate, the main fast excitatory neurotransmitter in the brain, carries a negative charge, and if narrow fusion pores are cation selective, this would imply that release of glutamate requires more dilated fusion pores, with implications for the speed of synaptic transmission in the central nervous system. This would fundamentally change present concepts of transmitter release through the fusion pore.

Electrodiffusion theory (Goldman, 1943; Alvarez and Latorre, 2017) predicts how the rate of catecholamine release through a fusion pore depends on the free ion concentrations in the extracellular medium and the vesicular lumen, the ionic permeabilities of the fusion pore (Gong et al., 2007), and the voltage that is present across the fusion pore (i.e., the intravesicular versus extracellular potential). To determine if fusion pores are cation selective, we performed anion substitution experiments and measured the rate of catecholamine release through fusion pores from chromaffin granules by quantifying the magnitude of amperometric foot currents (I_{foot}) and compared the results with the predictions from electrodiffusion theory. We also performed molecular dynamics (MD) simulations to assess the ratio of anion to cation permeation through fusion pores.

RESULTS

Electrodiffusion calculations and predictions

Nernst-Planck electrodiffusion theory was applied assuming a constant field across the fusion pores, as in Goldman-Hodgkin-Katz constant field theory (Goldman, 1943). For permeant ions, we assume that their fusion pore permeabilities are proportional to their bulk

diffusion coefficients (Gong et al., 2007), which seems justified because the fusion pore is large enough to allow permeation of large organic cations such as adrenaline (MW183 D).

The current I_S carried by ion S through a cylindrical fusion pore with length l and cross-sectional area a is given by

$$I_S = -D_S \cdot \frac{a}{l} \cdot z_S^2 \cdot \frac{VF^2}{RT} \cdot \frac{[S_V] - [S_E]exp(-z_S VF/RT)}{1 - exp(-z_S VF/RT)}, \quad \text{(Equation 1)}$$

where D_S is the diffusion coefficient for ion S, z_S is its valency, and $[S_V]$ and $[S_E]$ are its respective vesicular and extracellular concentrations. V is the voltage across the fusion pore, F is Faraday's constant, R is the gas constant, and T is absolute temperature. The conductance of the fusion pore can be used to substitute its geometric parameters

$$G_P = \sigma \cdot a/l, \quad \text{(Equation 2)}$$

where σ is the conductivity of the solution inside the fusion pore, giving

$$I_S = -D_S \cdot \frac{G_P}{\sigma} \cdot z_S^2 \cdot \frac{VF^2}{RT} \cdot \frac{[S_V] - [S_E]exp(-z_S VF/RT)}{1 - exp(-z_S VF/RT)}, \quad \text{(Equation 3)}$$

which is a more general representation for fusion pores with arbitrary non-cylindrical and dynamically changing geometry (Lindau and Gomperts, 1991). For the NaCl-based bath solution, the conductivity of the solution filling the fusion pore is approximately σ = 15 mScm^{-1}, and the quantity G_P/σ was calculated for a fusion pore conductance of G_P = 170 pS to be 1.13 × 10^{-8} cm. The voltage dependence of the partial current carried by catecholamines is shown as the red line in Figure 1A. The green line shows the corresponding amperometric current, which is twice as large because for each monovalent catecholamine (CA^+) two electrons are transferred in the amperometrically measured oxidation reaction.

The extracellular and intravesicular free ion concentrations and their diffusion coefficients are listed in Table S1. Although the extracellular concentrations are well defined in the experiment, the intravesicular concentrations of free Na^+ and K^+ were both assumed to be ~20 mM, and free Ca^{2+} and Mg^{2+} were assumed to be negligible (Haigh et al., 1989). The intravesicular free anion concentrations are unknown, but previous experiments revealed that during the amperometric foot signal (i.e., during release through a narrow fusion pore), there is no co-release of anions with catecholamine release (Gong et al., 2007). Therefore, the intravesicular free anion concentration was set to zero. The intravesicular free catecholamine concentration $[CA^+]_{free}$ was set to 200 mM to reproduce approximately the mean I_{foot} measured in the 140 mM NaCl-based solution. The calculated voltage dependence of the net current for a fusion pore that is permeable to all ions according to their diffusion coefficients is shown as the solid blue line in Figure 1A.

When a fusion pore opens, there may be voltage present across the fusion pore because the intravesicular potential may differ from the extracellular potential. This potential difference is discharged by a current through the fusion pore with a time constant

$$\tau = C_V / G_P,$$

(Breckenridge and Almers, 1987), where C_V is the vesicle capacitance. For a typical bovine chromaffin granule with a capacitance of ~2 fF and an initial fusion pore conductance >10 pS, the time constant is <200 μs. Thus, within less than 200 μs, the vesicle is discharged. Following this discharge, the intravesicular potential is, however, not equal to the extracellular potential but is set to the fusion pore zero current potential, which equals the liquid junction potential between intravesicular and extracellular solutions. The intravesicular potential can, accordingly, be calculated using the generalized Henderson equation (Barry and Lynch, 1991). For the normal NaCl-based solution, the zero current potential is −22 mV (Figure 1B, left panel) and is indicated by the solid blue vertical arrow in Figure 1A. I_{foot} at this potential (Figure 1A, green line) is indicated by the horizontal arrow labeled “I-foot 140 NaCl.” During the foot current, only a small fraction of catecholamines is released from the vesicle, such that the intravesicular ion concentrations and the intravesicular potential remain virtually constant during the duration of the foot.

When 140 mM NaCl in the bath solution is replaced by 140 mM NaGlu and the fusion pore is anion permeable, the net current-voltage relation changes as indicated by the dashed blue line in Figure 1A, and the zero current potential shifts to 8 mV (Figure 1A, dashed blue vertical arrow) because the mobility of Glu^- is only one quarter the mobility of Cl^- (Gerhardt and Adams, 1982; Ng and Barry, 1995; Hille, 2001). At this potential, I_{foot} is expected to be ~30% larger than at −22 mV (Figure 1A, horizontal arrow labeled “I-foot 140 NaGlu”). For an anion-permeable fusion pore, we thus expect that the foot currents increase by ~30% when NaCl is substituted by NaGlu.

For a fusion pore that is completely impermeable to anions, the net current-voltage relationship can be calculated setting the apparent diffusion coefficients for Cl^- or Glu^- to zero. In this case (Figure 1A, black line) the current-voltage relationship is unaffected by the anion substitution. The zero current potential (Figure 1A, vertical black arrow) is constant near +3 mV (Figure 1B, right panel), regardless of anion mobility. I_{foot} at this potential (Figure 1A, horizontal black arrow labeled “cation selective fusion pore”), and thus the rate of transmitter release, is expected to be 66% larger than that for an anion-permeable fusion pore in normal Cl^--based solution (Figure 1A, horizontal arrow labeled “I-foot 140 NaCl”). Cation selectivity of the fusion pore thus accelerates release of cationic neurotransmitters.

Amperometric foot current recordings reveal cation selectivity of small fusion pores

To determine if I_{foot} increases when NaCl is substituted by NaGlu, individual release events from bovine chromaffin cells were measured amperometrically using a CFM. Cells were stimulated either by intracellular application of 10 μM free Ca^{2+} through a whole-cell patch pipette or by extracellular application of ionomycin from an ejection pipette. Results from a whole-cell patch clamp experiment are shown in Figure 2. Amperometric spikes were recorded in subsequent sweeps of 120 s duration. To avoid any long-term effects secondary to substituting Cl^- with Glu^-, recordings were started in standard NaCl-based buffer (Figure 2A). In this cell, infusion of 10 μM free Ca^{2+} stimulated a very large number of release

events. During the second sweep, the batch solution was changed to the glutamate and the recording continued (Figure 2B). During later sweeps the solution was changed again three times to Cl^-, then to Glu^- and back to Cl^-.

Because of the high rate of release events, amperometric spikes were frequently overlapping, such that individual amperometric events were only analyzed to determine I_{foot} because quantal size (integral of amperometric spike), amperometric spike amplitude, and half-width could not be reliably quantified. I_{foot} was defined as the mean foot current during the duration of the foot signal (Figures 2A and 2B) (Mosharov and Sulzer, 2005). The largest foot current recorded in this cell is shown in Figure S1. The start of the foot signal is the last time point before the current deviates from the background level. The end of the foot signal is indicated by the transition to a steep rise of the amperometric current and quantified by extrapolating the linear fit of the rising slope to the baseline of the spike (Mosharov and Sulzer, 2005). I_{foot} reflects the low rate of catecholamine release through a fusion pore with conductance < 1 nS (Gong et al., 2007) and is proportional to the partial CA^+ current out of the fusion pore. The rapid rise of the amperometric spike marks the transition from a fusion pore to a large orifice, allowing more rapid transmitter release.

If a narrow fusion pore is cation selective, one would expect that a more dilated fusion pore eventually becomes anion permeable and all ions will permeate according to their bulk diffusion coefficients. We therefore constructed cumulative distributions of I_{foot} in the two different solutions for individual cells to avoid obscuring effects from cell-to-cell variability. The cumulative distribution measured in Glu^--based solution (Figure 2C, red line) is shifted to larger foot currents compared with that of foot currents measured in Cl^--based solution (Figure 2C, blue line) for somewhat dilated fusion pores with foot currents >1 pA, but for narrow fusion pores that generate foot currents < 1 pA, the cumulative distributions are indistinguishable. Narrow fusion pores with low conductance and small foot current therefore appear to be insensitive to anion substitution, suggesting that they are impermeable to anions, while more dilated fusion pores become increasingly permeable to anions with a transition from a cation-selective fusion pore to a fusion pore that allows anion permeation beginning around 1 pA foot current.

On the basis of electrodiffusion theory, amperometric foot currents are expected to increase by ~30% when extracellular Cl^- is replaced by Glu^- (Figure 1A) if the fusion pore is fully permeable to anions ($P_{Cl}/P_K = 1$). To determine the cumulative I_{foot} distributions on the basis of that expectation, all individual I_{foot} values measured in Cl^- were multiplied by a factor of 1.3. The resulting expected cumulative distribution is shifted to higher I_{foot} values (Figure 2C, green line). In contrast, amperometric foot currents would be unchanged if the fusion pore is impermeable to anions ($P_{Cl}/P_K = 0$), and the cumulative distribution measured in Glu^- (Figure 2C, red line) would be identical to that measured in Cl^- solution (Figure 2C, blue line). Evidently, the frequency distribution of foot currents below ~1.2 pA (Figure 2C) is unchanged when Cl^- is substituted by Glu^- (red line), but the distribution begins to shift to larger foot currents above that threshold. For large foot currents, the shift approaches that expected for an anion-permeable fusion pore (Figure 2C, green line). The distributions obtained in Cl^--based solution and in Glu^--based solution were significantly different ($p = 0.041$, Kruskal-Wallis test).

As an alternative stimulation method, chromaffin cells were stimulated by extracellular application of 10 μM ionomycin from a puffer pipette. In these experiments the solution was exchanged between recordings from individual cells, and amperometric spike distributions were obtained pooling the data from multiple cells and multiple preparations. As for intracellular Ca^{2+} stimulation, the cumulative I_{foot} distribution was unchanged when Cl^- was substituted by Glu^- for small foot currents but deviated for larger foot currents. The distribution was shifted to larger foot currents for more expanded fusion pores with a transition point for divergence of the distributions at ~1.6 pA (Figure 3A), further supporting the evidence that narrow fusion pores are cation selective but expanded fusion pores are also permeable to anions. The shift again approaches that expected for an anion-permeable fusion pore (Figure 3A, green line). These results indicate that that with both types of stimulation, the narrow fusion pores are impermeable to anions, but anion permeability increases when the fusion pores expand.

When amperometric spike parameters from multiple cells are pooled, the effect of cell-to-cell variability must be taken into account. We therefore performed the statistical analysis using the cell preparation and individual cell identifier as nested random variables. The amperometric spike parameters and their statistical analysis are provided in Figure S2. The mean I_{foot} increased by ~35% from 3.23 ± 0.36 to 4.45 ± 0.36 pA ($p = 0.02$). When the foot currents in the ranges below and above the 1.6 pA threshold are analyzed separately, there are no differences between the mean values in the two different solutions for small foot currents (Figure 3B), while for an anion-permeable fusion pore, I_{foot} would be expected to increase by ~30%. If this were the case, the mean foot currents in this range would be expected to increase by 30% (Figure 3B, bar labeled Clx1.3). The mean I_{foot} value in the low range measured in Glu^--based solution is clearly inconsistent with this expected change, providing further evidence that narrow fusion pores are impermeable to anions. For the more expanded fusion pores, the mean I_{foot} increases in Glu^--based solution compared with that in Cl^--based solution as expected for a nonselective fusion pore (Figure 3C).

Quantitative analysis of I_{foot} distributions

To quantitatively account for the gradual transition from cation selective to unselective, the results were fitted on the basis of a relation between anion permeability and fusion pore conductance, or the equivalent I_{foot}. For this purpose, we assumed that the permeability of Cl^- relative to that of K^+ (R) depends on the fusion pore conductance G_P as

$$R = \frac{P_{Cl}}{P_K} = \frac{1}{1 + (G_{1/2}/G_P)^n}. \quad \text{(Equation 4)}$$

$G_{1/2}$ is the fusion pore conductance where R equals one-half and the exponent n determines the steepness of the transition. Equation 4 provides a sigmoid curve for R rising from zero at small G_P to one at large G_P.

The relation between I_{foot} in Glu^- solution ($I_{foot,Glu}$) and I_{foot} in Cl^- solution ($I_{foot,Cl}$) may be approximated by the relation

$$I_{foot,\ G/u} = I_{foot,Cl} \cdot (1 + R \cdot (1.3 - 1)), \quad \text{(Equation 5)}$$

which provides a transition of foot current scaling factor from 1 at small anion permeability (no change) to 1.3 (30% increase) at high anion permeability.

With $I_{\text{foot,Cl}}$ being proportional to G_P, we rewrite Equation 4 as

$$R = \frac{1}{1 + \left(I_0 / I_{foot,Cl}\right)^n}. \quad \text{(Equation 6)}$$

I_0 is the average foot current in Cl^--based solution where the permeability ratio R equals one-half. It should be noted that here G_P is the fusion pore conductance in normal Cl^--based solution and is as such a measure of fusion pore geometry. Substituting Equation 6 in Equation 5, we obtain

$$I_{foot,G/u} = I_{foot,Cl} \cdot \left(1 + \frac{1.3 - 1}{1 + \left(I_0 / I_{foot,Cl}\right)^n}\right). \quad \text{(Equation 7)}$$

According to Equation 7, $I_{\text{foot,Glu}}$ will be equal to $I_{\text{foot,Cl}}$ for $I_{\text{foot,Cl}} \ll I_0$ and approach 1.3 3 $I_{\text{foot,Cl}}$ for $I_{\text{foot,Cl}} \gg I_0$.

To determine how the cumulative frequency distribution relates to such a model, the distribution obtained in Glu^- solution was fitted using a more general version of Equation 7. In this generalized form (Equation 8), we allow the change in foot current for large fusion pores to differ from the fixed factor of 1.3 because once the fusion pore allows for anion permeation, the entry of Glu^- may further modify fusion pore properties

$$I_{foot,G/u} = I_{foot,Cl} \cdot \left(1 + \frac{S - 1}{1 + \left(I_0 / I_{foot,Cl}\right)^n}\right), \quad \text{(Equation 8)}$$

where S is the scaling factor of amperometric foot current for a larger fusion pore. Fitting the data of Figure 2C on the basis of Equation 8 is not trivial, because essentially the frequency distribution values for Glu^- solution are related to those measured in Cl^- solution. Equation 8 is of the form

$$I_{foot,G/u} = F\left(I_{foot,Cl}\right). \quad \text{(Equation 9)}$$

For the transformation of the distribution measured in Cl^- solution to that measured in Glu^- solution, we need to determine the $I_{\text{foot,Cl}}$ values that correspond to given $I_{\text{foot,Glu}}$ values. We thus would need to solve for $I_{\text{foot,Cl}}$ to obtain an expression of the form

$$I_{foot,Cl} = G\left(I_{foot,G/u}\right). \quad \text{(Equation 10)}$$

As Equation 8 is a nonlinear equation that cannot be solved for $I_{foot,Cl}$ analytically, the $I_{foot,Cl}$ values that correspond to given $I_{foot,Glu}$ values were found numerically according to Equation 8, using the FindRoots operation implemented in Igor Pro, which allowed fitting the numerically inverted Equation 8.

The cumulative I_{foot} distributions obtained in Glu^- solution were fitted well on the basis of Equation 8 (Figures 2C and 3A, black dashed lines). For intracellular application of 10 μM free Ca^{2+} via a patch pipette in the whole-cell configuration (Figure 2C), the resulting fit provided a scaling factor $S = 1.35 \pm 0.02$, close to the 1.3 expected from electrodiffusion theory, a parameter $I_0 = 0.94 \pm 0.04$ pA, and an exponent $n = 8.0 \pm 2.2$, indicating a rather steep transition. For ionomycin stimulation (Figure 3A), the fit provided a scaling factor $S = 1.26$, again close to the 1.3 expected from electrodiffusion theory, a parameter $I_0 = 2.8$ pA and an exponent $n = 2.7$. The corresponding curve for the change in anion permeability R from 0 to 1 (Equation 6), shown in Figure 3D, is more shallow, presumably reflecting cell-to-cell variability. On the basis of the average fusion pore conductance/catecholamine flux ratio in bovine chromaffin cells of ~140 pS pA^{-1} (Gong et al., 2007), the relation between anion permeability and I_{foot} was converted to a relation between anion permeability and fusion pore conductance with $I_0 = 2.8$ pA corresponding to ~390 pS (Figure 3D, top scale).

MD simulations reveal the mechanism of fusion pore selectivity

To obtain insight into the molecular mechanism of fusion pore cation selectivity, ion permeation was analyzed in coarse-grained MD (CGMD) simulations of an arrangement of four SNARE complexes bridging a nanodisc and a planar membrane, where fusion pores formed spontaneously (Sharma and Lindau, 2018b) (Figure 4A). From these simulations, the fusion pore permeation of cations (blue) and anions (red) was quantified. As shown in the trajectories (Figure 4B), most anions do not traverse the narrow part (shaded yellow in Figures 4A and 4B) of the fusion pore. In all simulations in which cation permeation was detected, the number of permeating anions was either zero or much smaller than the number of permeating cations (Figure 4C; Table S2). The experimental results revealed that fusion pore selectivity varies with fusion pore conductance. We therefore investigated if such a dependence is also evident in the simulations.

The conductance of a fusion pore appearing in the simulations can be estimated on the basis of fusion pore geometry and the conductivity of the solution inside the fusion pore ($\boldsymbol{\sigma}$ = 15 $mScm^{-1}$) (Sharma and Lindau, 2018b). The fusion pore geometry and therefore its conductance fluctuate during the simulations. When the average fusion pore conductance of individual simulations was estimated (Figure 4C, bottom axis) it became evident that the permeability ratio $R = P_{anion}/P_{cation}$ increases with increasing fusion pore conductance (Figure 5A, black markers). A fit with Equation 4 (black line) yielded $G_{1/2} = 587 \pm 15$ pS and a steepness exponent $n = 6.6 \pm 0.8$.

For narrow pores, however, there is a reduced water diffusion coefficient because of interactions of the water molecules with the walls of the pore, reducing the conductance of the pore. The reduction of water self-diffusion can be estimated by comparing the diffusion distances of water inside the pore along its long axis with those of bulk water far away from

the pore (Smart et al., 1998), an approach that was also applied to fusion pore simulations (Sharma and Lindau, 2018b). This reduced diffusion of water and ions in a narrow pore leads to a correction factor, reducing the fusion pore conductance estimate compared with that based on bulk solution conductivity alone. Figure 5B (gray dots) shows the relation between corrected and uncorrected fusion pore conductance (5 ns averages) from all four independent fusion pore simulations with open time intervals >25 ns. The relation between corrected G_P and uncorrected G_P was fitted (black line) using the function

$$G_{P,\,corrected} = \frac{G_{P,\,uncorrected}}{\left(1 + \left(G_0/G_{P,\,uncorrected}\right)^n\right)}, \qquad \text{(Equation 11)}$$

which assumes that the correction factor approaches a value of 0 for infinitesimally small fusion pores (no water/ion permeation) and a value of 1 for very large fusion pores (no correction compared with bulk diffusion). The resulting fit parameters G_0 = 1,305 ± 41 pS and n = 1.43 ± 0.07 were then used to correct the averaged fusion pore conductance values (Figure 5A, blue markers). The fit with Equation 4 (blue line) yielded $G_{1/2}$ = 143 ± 8 pS and n = 3.0 ± 0.4.

The CGMD simulations were performed using the Martini force field, which combines four non-hydrogen atoms into one Martini bead. Martini water beads thus group four water molecules into a single bead, which reduces thermal fluctuations, smoothens the potential energy surface, and increases the simulation time step, enabling longer timescale simulations. Although Martini-based CGMD simulations can capture all major bulk properties of membranes, they may not be appropriate for narrow and constricted pores, as studied here, because of the larger bead size, simpler interaction potential, and the loss of entropy (Bennett and Tieleman, 2011). Two configurations from CGMD simulations were therefore converted to an atomistic (AT) representation, and a 25 ns AT simulation was performed for each of them, comparing the diffusion-corrected and uncorrected conductance estimates from the last 19 ns of these simulations (Figure 5B, red circles). The fit with Equation 11 provided the parameters G_0 = 683 ± 15 pS and n = 3.4 ± 0.6, which were then used to correct the fusion pore conductance values (Figure 5A, red markers). The fit with Equation 4 (Figure 5A, red line) yielded $G_{1/2}$ = 236 ± 20 pS and n = 1.7 ± 0.2. It should be noted that the fusion pores obtained in MD simulations have a relatively low conductance because the small size of the nanodisc, which represents a small area of the vesicle membrane, limits the ability of the fusion pore to expand. The larger fusion pores in the simulations exhibit therefore still considerable cation selectivity. The fits using Equation 4 are nevertheless justified because in a widely expanded fusion pore, the permeating ions do not interact significantly with the pore walls, and their diffusion can thus be assumed to equal that in bulk solution.

In summary, the simulations also indicate that small fusion pores are cation selective and that anion permeability gradually increases as the fusion pore expands. The estimates for the transition where P_{Cl}/P_K reaches 0.5 range from 590 pS for uncorrected conductance to 240 pS for diffusion-corrected conductance and 140 pS for coarse-grained corrected conductance.

DISCUSSION

Understanding the transmitter electrodiffusion properties and permeation of the fusion pore is necessary for revealing the dynamics for transmitter release, synaptic transmission, and ultimately the function of the nervous system. Many neurotransmitters are organic ions, which carry positive or negative charge, and their fusion pore permeation must therefore be treated as an electrodiffusion process. It has been shown that for narrow fusion pores there is no significant co-release of anions associated with catecholamine release from chromaffin granules and that charge compensation occurs by entry of Na^+ ions via the fusion pore (Gong et al., 2007). Here we show by ion substitution experiments in amperometric recordings of individual fusion events as well as CGMD simulations of SNARE-mediated fusion pores that narrow fusion pores are cation selective, while more dilated fusion pores are not. Estimates from the experimental data for the fusion pore conductance where P_{Cl}/P_K reaches 50% in the transition from a cation selective to a nonselective fusion pore are in the range 140–390 pS, corresponding to an I_{foot} range of ~1.0–2.8 pA in bovine chromaffin cells.

The structural basis for cation selectivity of the fusion pore

To gain insight into the structural basis for the cation selectivity, ion permeation through fusion pores involving four SNARE complexes was investigated using CGMD simulations, complemented by AT simulations of selected fusion pore states. Consistent with the experimental data, the analysis of the simulations revealed that fusion pores with small conductance allow only for permeation of cations and that fusion pores with higher conductance become progressively anion permeable. The estimates from the simulations for the fusion pore conductance where P_{Cl}/P_K reaches 50% in the transition from a cation-selective to a nonselective fusion pore are in the range 140–590 pS, with 590 pS likely being a considerable overestimate because this value did not take into account the reduced diffusion in a narrow pore due to interactions of water molecules and ions with the pore wall (Smart et al., 1998). The estimates obtained in the simulations are therefore in very good agreement with those obtained experimentally.

The cation selectivity of narrow fusion pores is presumably due to the presence of negative charges lining the fusion pore. It has become increasingly clear that the transmembrane domains of the SNARE proteins synaptobrevin 2 and syntaxin 1 play an important role in the formation of the fusion pore (Ngatchou et al., 2010; Chang et al., 2016; Dhara et al., 2016), which is a highly dynamic proteo-lipid structure (Fang et al., 2008; Bao et al., 2016; Sharma and Lindau, 2018b).

For a better understanding of the cation selectivity, the CGMD simulations were further analyzed to identify the negative charges lining the fusion pore. The C termini of the SNARE transmembrane domains pointing into the core of the fusion pore (Sharma and Lindau, 2018b) contribute negative charges lining the fusion pore. In addition, about equal amounts of negative charge are contributed from negatively charged lipids (Table S2). About 50–70 lipid head groups line the fusion pore, contributing ~7–9 negative charges, while the C termini of the SNARE TM domains contribute ~4–7 negative charges. These results indicate that negatively charged lipids as well as the SNARE TM domain C

termini contribute to cation selectivity. It should be noted, however, that the density of negatively charged lipids lining the fusion pore will depend on the exact lipid composition. In the simulations performed here, every effort was made to simulate a membrane with physiological composition and leaflet asymmetry such that only few negatively charged lipids were present in the extracellular and intravesicular leaflet (Sharma et al., 2015).

The electrostatic potential inside the fusion pore

For a more mechanistic understanding of the cation selectivity, we investigated the electrostatic potential, the locations of negative charges lining the pore, and the locations of ions inside two fusion pores with different conductances (Figure 6), one with very small conductance (Figure 6A, 290 pS uncorrected, 13 pS diffusion corrected) and the other with larger conductance (Figure 6B, 630 pS uncorrected, 290 pS corrected). In the simulations we find a region around the extracellular mouth of the fusion pores with a high negative charge density, contributed primarily by the C termini of the SNARE TM domains and three PIP2 head groups that are located in the same area (Figures 6A and 6B, top panels, arrows). The electrostatic potential along the pores (Figures 6A and 6B, bottom panels) contains contributions from both, the negative charges from SNAREs and lipids, and the ions present in the fusion pore.

The locations of the charges from lipids and proteins in the two fusion pores are shown in Figure 7A. As expected, the negative charges from the SNARE C termini and PIP2 are located in a region around the extracellular mouth of the fusion pore (z = 45–90 Å). Negative charges from PS lipids are rather homogeneously distributed along the fusion pore. No negative ions are present inside the pore. Cations are accumulated around the cluster of negative charges. In the low-conductance fusion pore, a sharp peak in cation density is specifically colocalized with the negative charges from Stx1 and PIP2 (Figure 7A, panel cations). The sharp peak indicates that the cations (and water) in the fusion pore are rather immobile on the timescale of 10 ns, explaining the very low diffusion-corrected conductance estimate of ~13 pS.

These results suggest that PIP2 headgroups and the Stx1 C termini contribute to the selectivity filter. The simulations show that PIP2 contributes to the stabilization of cations at the extravesicular mouth of the fusion pore. Absence of phosphatidylinositol-4-phosphate 5-kinase (PIPKIγ) caused a reduction of PIP2 levels in chromaffin cells and a delay in fusion pore expansion (Gong et al., 2005), suggesting that PIP2 accelerates fusion pore expansion, but a possible dependence of the magnitudes of foot currents in PIP2 has not been studied. It would be interesting to investigate if a reduction of PIP2 levels in chromaffin cells changes the cation selectivity of narrow fusion pores.

The mean electrostatic potential profile (Figure 7A, bottom panel) includes the field from the ions present in the fusion pore, as in the single snapshot (Figure 6, bottom panel). When the electrostatic potential is calculated omitting the contributions from the dissolved ions, the profiles shown in Figure 7B are obtained. It should be noted that these are hypothetical curves because fusion pores immediately collapse when the ions are removed and the simulation is continued in their absence. Nevertheless, the curves show a pronounced negative potential well inside the fusion pores, which is much deeper for the fusion

pore with low conductance than for that with higher conductance, consistent with the accumulation of cations in this region (Figure 7A, panel cations).

A possible function of cation-selective fusion pores

An anion-impermeable fusion pore has a more positive zero current potential accelerating release of positively charged transmitters, as shown here for chromaffin cells which release positively charged catecholamine (Figure 1). Revealing the characteristics of the fusion pore through models of electrodiffusion calculations can enhance our predictions and understanding of different physiological conditions releasing charged transmitter. Fusion pore formation in small synaptic vesicles is achieved by the same molecular machinery composed of synaptobrevin 2, syntaxin 1, and SNAP-25, and the fusion pore selectivity features described here will thus also apply to fusion pore formation and transmitter release from small synaptic vesicles. A consequence of cation selectivity will be an acceleration of acetylcholine release through a narrow fusion pore at the neuromuscular junction, thereby maximizing the speed of release, or a more rapid elevation of catecholamine levels in blood to quickly respond to stress. On the other hand, release of glutamate, the major excitatory transmitter in the brain, may require a more extended fusion pore. In chromaffin cells, a subset of fusion pores expands very rapidly, possibly those formed at locations of SNAP-25 clusters (Zhao et al., 2013; Shin et al., 2018). Alternatively, it may require less net negative charge in the fusion pore. The net negative charge could be modulated by the number of SNARE TM domains involved in fusion pore formation as well as lipid composition or by other molecules that contribute positive charges and may increase the rate of release of these negatively charged neurotransmitters.

STAR★METHODS

RESOURCE AVAILABILITY

Lead contact—Further information and requests for resources should be directed to and will be fulfilled by the Lead Contact, Manfred Lindau (ML95@cornell.edu).

Materials availability—This study did not generate new unique reagents.

Data and code availability—Amperometry and computational data reported in this paper will be shared by the lead contact upon request. DOIs are listed in the key resources table. Any additional information required to reanalyze the data reported in this paper is available from the lead contact upon request.

EXPERIMENTAL MODEL AND SUBJECT DETAILS

Buffer A contained (in mM) 118 NaCl, 3.3 KCl, 1 $NaH_2PO_4.H_2O$ (CHEBI: 37585, cat no.: 7892, Mallinckrodt Chemicals), 1 $MgSO_4.7H_2O$ (CHEBI:32599, cat no.: M63–500, Fisher Scientific), 10 glucose, 25 HEPES-NaOH, 2 L-Glutamine (CHEBI: 18050, cat no.: 25030–081, GIBCO), 100 units-mg/mL Pen-Strep (cat no.: 15140–122, GIBCO), 0.1 mg/mL Gentamycin (CHEBI: 102135, cat no.: 15750–060, GIBCO), supplemented with MEM vitamins (cat no.: 11120–052, GIBCO) and MEM amino acids (cat no.: 11140–050, GIBCO) according to manufacturer's instructions. Buffer B was equal to buffer A

supplemented with 0.1% Bovine Serum Albumin Fraction V (BSA, cat no.: A7906, Sigma-Aldrich) and "collagenase buffer" was equal to buffer B supplemented in addition with 1 mg/mL collagenase.

Bovine chromaffin cells were prepared as described (Parsons et al., 1995; Huang et al., 2019) in accordance with an IACUC approved protocol (1999–0015). Adrenal glands were obtained from a freshly slaughtered cow and placed in buffer A on ice for transportation. After arrival at the lab, fat was immediately cut away with sterile surgical blades, and the glands perfused, digested, and cells prepared as described (Huang et al., 2019). Depending on cell concentration, a volume of the dissociated chromaffin cell suspension was plated on 8 mm diameter glass coverslips treated with 0.02% poly-D-lysine, to achieve an average cell separation distance > 25 μm. Pyrex cell culture Petri dishes held 5–7 glass coverslips, and after cells adhered to the glass coverslips, 1.5 mL of cell media was added to cover the entire Petri dish. The cells were kept in an incubator with 8% CO_2, in culture media containing (in mL) 200 Dulbecco's modified eagle medium/nutrient mixture F-12 (cat no.: 10565–018, GIBCO), 200 Ham's nutrient mixture F-12 (cat no.: 11765–054, GIBCO), 40 fetal bovine serum (cat no.: 16000–044, GIBCO), 4 Pen/strep, 4 L_Glutamine (0.2 M), 9 HEPES/NaOH (1M), 4.6 Insulin-Transferrin-Selenium-Ethanolamine (100X, cat no.: 51500–056, GIBCO). Cells were used for amperometric recordings 24 hours after preparation for up to one week. Generally, the most active days for chromaffin cell batches were 2 days after preparation.

For experiments, individual coverslips with cultured cells were removed from the incubator and placed in a recording chamber with extracellular bath solution. Bath solutions contained either 140 mM NaCl or 140mM Na D-Glutamate (NaGlu) plus (in mM) 5 KCl, 5 $CaCl_2$, 1 $MgCl_2$, 10 HEPES/NaOH, with a pH of 7.3 and osmolarity adjusted to ~325mmol/kg with ~20 mM D-glucose. Solution exchange was performed using a suction pump while new solution was provided to the recording chamber via gravity flow. Some loose cells were removed from the dish by the bath perfusion. Remaining healthy cells firmly attached to the coverslip were chosen for single cell recording. After transfer to the set-up cells were used for up to 1 hour. Experiments were performed at room temperature.

METHOD DETAILS

Intracellular calcium stimulation—Cells were stimulated by intracellular application of 10 μm free Ca^{2+} in the whole cell patch clamp configuration with a pipette solution containing (in mM) 110 CsGlutamate, 8 NaCl, 20 diethylenetriaminepentaacetic acid (DTPA), 5 $CaCl_2$, 2 MgATP, 0.3 Na_2GTP, 40 HEPES, adjusted to pH 7.4 with CsOH, and osmolarity of ~325mmol/kg. Patch pipettes were fabricated from borosilicate glass capillaries (1.8 mm o.d., Hilgenberg GmbH, Germany) with a P-97, pipette puller (Sutter Instrument, Novato, CA) and fire polished to a resistance of 3–5MΩ. Cells were voltage clamped at a constant holding potential between −60 and −70 mV (without liquid junction potential correction) using an EPC10 double amplifier (HEKA, Lambrecht, Germany) and amperometric current and whole cell holding current were recorded simultaneously. The reference electrode was an agarose bridge electrode filled with 3M KCl.

After establishing the whole cell configuration in standard NaCl based buffer, the recordings were started with repeated sweeps of 120 s duration. Bath solution was changed to NaGlu

based buffer using the gravity-based system. According to the time course of a small change of holding current during the solution exchange, the solution change took less than 10 s. To ensure complete solution exchange, the wash was performed for 20–50 s. Solution was switched multiple times until the rate of amperometric spikes became negligible or the holding current increased indicating that the seal became leaky.

Extracellular ionomycin stimulation—For ionomycin experiments, the extracellular solution was changed every 10 minutes, altering between control (NaCl) and NaGlu based solution. Recordings were performed positioning the CFM near (< 2 μm) a chromaffin cell and applying +650 mV versus an Ag|AgCl reference electrode with an EPC-8 amplifier (HEKA, Lambrecht, Germany) filtered at 1 kHz using the built-in filter. Fusion events were stimulated by pressure ejection of NaCl based bath solution containing 10 μM ionomycin from an ~5 μm diameter micropipette tip located ~25 μm away from the cell using an MPCU bath handler (Lorenz, Katlenburg-Lindau, Germany). To allow for sufficient dilution, solution flow was directed to pass the cell on the side and very low pressure was applied (5 cm H_2O), generating a measured flow rate of ~300 pL/s. Amperometric recordings were started 60 s before stimulation, followed by 120 s of recording during ejection of the ionomycin solution and continued for another 280 s after ejection was stopped.

Amperometric recordings—Amperometry was performed using custom made CFMs (Berberian et al., 2009). A single carbon fiber (5 μm diameter) was inserted in a borosilicate glass capillary (1.8 mm o.d., Hilgenberg GmbH, Germany), which was then pulled using a P-97 pipet puller. CFM tips were dipped in melting wax (Sticky Wax, Kerr Corporation, Brea, CA) for 2 min and subsequently cut using a blade (no. 10, Feather Safety Razor Co., Japan). For experiments, CFMs were backfilled with 3 M KCl solution. Recordings were analyzed by a customized macro (Mosharov and Sulzer, 2005) for Igor software (WaveMetrics, Lake Oswego OR) determining for each event maximum current amplitude, half-width, and quantal size measured as the area underneath the spike of interest. Pre-spike foot currents were quantified as mean of foot current magnitude (I_{foot}) and foot duration (t_{foot}). Analysis of fusion pore foot signals was restricted to $I_{foot} > 0.5$ pA and $t_{foot} > 2$ ms. All experiments were performed at room temperature.

Coarse-grained molecular dynamics simulation—The starting configuration for fusion pore simulations was a MARTINI coarse-grained representation (Marrink et al., 2007; Monticelli et al., 2008) composed of a ~29 nm x 29 nm planar bilayer and a ~13 nm nanodisc (ND) mimicking a patch of the synaptic vesicle membrane, bridged by four partially unzipped trans-SNARE complexes based on PDB entry 3HD7 (Stein et al., 2009), generated as described (Sharma and Lindau, 2018b). The composition of the planar plasma membrane was based on the experimentally determined lipid composition of rat brain synaptosomal plasma membrane (Breckenridge et al., 1972) with asymmetric lipid composition in the two leaflets formed by a self-assembly approach (Sharma et al., 2015). The nanodisc (ND) was prepared using a scaffold protein based on variant MSP1E2 of membrane scaffold protein 1 (MSP1) (Borhani et al., 1997) and filled with a patch of self-assembled membrane with lipid composition based on synaptic vesicle (SV) lipid composition (Takamori et al., 2006).

All simulations were carried out using GROMACS 4.5.x (Van Der Spoel et al., 2005) and visualized using VMD (Humphrey et al., 1996). The CG simulations used standard martini CGMD parameters. Non-bonded interactions were cut off at 1.2 nm distance. The Lennard Jones potential was shifted from r = 0.9 nm to the cutoff distance. The time step used to integrate the equations of motion was 20 fs. Temperature was maintained at 310 K using a relaxation time of 1 ps and pressure at 1.0 bar using semi-isotropic coupling, with 1 ps relaxation time using Berendsen methods (Berendsen et al., 1984).

Atomistic molecular dynamics simulation—To investigate in more detail the properties of nascent pore suggested by CGMD simulations, two atomistic simulations were performed. The starting structures of the simulations were taken from two different CGMD simulation trajectories (sim1, 1250 ns and Sim 11, 1152 ns). These states were converted to all-atom (atomistic, AT) structures using a fragment-based protocol (Stansfeld and Sansom, 2011). The generated atomic system was energy minimized and further subjected to three rounds of equilibration of 5 ns each. The first round was done for 5 ns to equilibrate water with all other heavy atoms restrained (force constant = 100 kJ/mol/Å^2). In the next round of a 5 ns equilibration, only the protein Cα atoms and the lipid head groups were restrained. In the last round of equilibration only the head groups of lipids that lined the pore region were restrained using a weaker force constant of 10 kJ/mol/Å^2. This was subsequently followed by an unrestrained production run of 25 ns. The atomistic simulations were carried out using the GROMOS96 force field (Scott et al., 1999) with the 53a6 force field (Oostenbrink et al., 2004). The force field parameters for glycolipids were taken from (Gu et al., 2017) with the head group parametrized based on the GROMOS hexopyranose force field (Lins and Hünenberger, 2005; Pol-Fachin et al., 2012). The parameters of other lipids were taken from (Kukol, 2009).

Atomistic simulations were performed using GROMACS 4.6.5 (Van Der Spoel et al., 2005; Hess et al., 2008). All simulations were carried out at 310 K constant temperature using V-rescale algorithm (Bussi et al., 2007) and semi-isotropic pressure coupling (1 bar) using the Parrinello-Rahman barostat (Parrinello and Rahman, 1981). Long-range electrostatic interactions were computed using the particle mesh Ewald (PME) method (Darden et al., 1993). All bonds were constrained employing the LINCS algorithm (Hess et al., 1997). The time step used for the simulations was 2 fs and the trajectories were saved every 20 ps. Most analysis can be performed using standard GROMACS tools and the visualized in VMD (Humphrey et al., 1996).

Fusion pore conductance estimates—In CG simulations fusion pore conductance was determined for all time periods where a continuous fusion pore existed for > 25 ns. In AT simulations fusion pore conductance was analyzed for the last 19 ns of the 25 ns production run. For both, CG and AT simulations, a cylindrical region of radius 3 nm was defined at the start of each nanosecond of analysis, with its z axis passing through the center of mass (COM) of T91 residues of all four Syb2 molecules. The upper bound of the fusion pore was defined by using the COM of Cα atoms (for AT simulations) or backbone beads (for CG simulations) of the membrane scaffold protein of the nanodisc, respectively, while the lower bound of the fusion pore was described using the COM of G288 residues of all

four Syntaxins. The fusion pore geometry was defined by the waters present inside this region. For both, CG and AT simulations, the mean square displacement (MSD) of waters was calculated using the GROMACS utility g_msd, at 1 ns intervals for each 0.45 nm slice along the z axis in the fusion pore region. The MSD of the waters inside the fusion pore was calculated and conductance determined using relations as described previously (Sharma and Lindau, 2018b).

Quantification of ion permeation in CGMD simulations—Analysis of ion permeation was done on the trajectory with frames dumped at time steps of 1 ns. The trajectories of the putative fusion pore boundaries, defined by the center of mass of backbone atoms (C-alpha in case of AT) of MSP (upper bound) and Gly100 residues of syntaxin 1 (lower bound), were saved. For all the ions that were within 2 nm of any T91 residue of synaptobrevin 2, at any point during the simulation, their z-coordinates along the trajectory were extracted and saved. The trajectory of each ion was then compared to the trajectory of the upper and lower bounds of the pore. An ion with z-coordinate below that of the upper bound was considered to enter the pore from the intravesicular region, provided that its z-coordinate was greater than the upper bound in the preceding frame. An ion with z-coordinate greater than that of the lower bound, with its z-coordinate less than the lower bound in the previous frame, was considered to enter the pore from the extracellular region. An ion that entered the pore was considered to permeate the pore if at any subsequent time point its z-coordinate was found to be outside the pore bound opposite to the side from which it had entered the pore.

Electrostatic potential calculations—The electrostatic potential was calculated using the last 10 ns of atomistic simulation trajectories of a large (292 pS) and a small (~13 pS) fusion pore (diffusion corrected conductances). The electrostatic potential was calculated for individual frames, 200 ps apart, and was performed employing the PMEPot module of the visualization program VMD (Humphrey et al., 1996) with a grid resolution of 1 Å and Ewald factor value of 0.25 $Å^{-1}$. For the panels shown in Figure 7, the 50 electrostatic potential maps of these snapshots were then averaged along the z axis over the pore. To define the pore for each frame, at first a rectangular volume of 6 × 6 × 17.7 nm^3, centered at the x- and y- coordinates of the center of mass of the SNARE C-termini, was considered. Next, within this volume the pore was further described by determining the solvent (water and ions) cluster in the fusion pore using single linkage algorithm with a cut-off of 7.5 Å. The solvent cluster was then also used to calculate the ion distribution along the fusion pore using a bin width of 1 Å. The distribution of lipid head group charges in the pore was calculated by considering their counts in the same rectangular volume.

QUANTIFICATION AND STATISTICAL ANALYSIS

Cumulative distributions of amperometric spike parameters were generated to determine possible differences in distribution of values and frequency with ion substitution. Cumulative foot current distributions in Cl^- and Glu^- solutions from single cell patch clamp experiments (Figure 2C) were compared using Kruskal-Wallace test (IGOR Pro).

For ionomycin stimulation, data were pooled from multiple cells and cell preparations to obtain a large sample size of fusion events. To account for different cell batches and cell-to-cell variability, *p-value*s for test of significance were determined through least square regression in JMP software (SAS, Cary, NC), with random effects accounted for by unique single cell identification nested in its respective animal adrenal gland source (cell preparation). I_{foot} distributions were independent of anion substitution for small foot currents (i.e., narrow fusion pores) but were changed for larger foot currents (more dilated fusion pores) with a threshold of ~1.6 pA. Therefore, foot currents in the range below 1.6 pA were elected for small foot currents, and foot currents greater than the respective threshold for large foot currents. These ranges were selected for separate statistical analysis using JMP software. Statistical data are expressed as mean ± s.e.m

Supplementary Material

Refer to Web version on PubMed Central for supplementary material.

ACKNOWLEDGMENTS

We are indebted to Dr. Wolfhard Almers for most valuable comments on the manuscript, and we thank Owasco Meat Co., Inc., for providing the bovine adrenal glands. This work was supported by National Institutes of Health grants R01 GM121787 and R01 GM085808, by European Research Council grant ADG 322699, and computational resources of the Max-Planck Society's Computing and Data Facility. J.B.D. was awarded a State University of New York Minority Fellowship.

REFERENCES

Aksimentiev A, and Schulten K (2005). Imaging alpha-hemolysin with molecular dynamics: ionic conductance, osmotic permeability, and the electrostatic potential map. Biophys. J. 88, 3745–3761. [PubMed: 15764651]

Albillos A, Dernick G, Horstmann H, Almers W, Alvarez de Toledo G, and Lindau M (1997). The exocytotic event in chromaffin cells revealed by patch amperometry. Nature 389, 509–512. [PubMed: 9333242]

Alvarez O, and Latorre R (2017). The enduring legacy of the "constant-field equation" in membrane ion transport. J. Gen. Physiol 149, 911–920. [PubMed: 28931632]

Bao H, Goldschen-Ohm M, Jeggle P, Chanda B, Edwardson JM, and Chapman ER (2016). Exocytotic fusion pores are composed of both lipids and proteins. Nat. Struct. Mol. Biol 23, 67–73. [PubMed: 26656855]

Barry PH, and Lynch JW (1991). Liquid junction potentials and small cell effects in patch-clamp analysis. J. Membr. Biol. 121, 101–117. [PubMed: 1715403]

Bennett WFD, and Tieleman DP (2011). Water defect and pore formation in atomistic and coarse-grained lipid membranes: pushing the limits of coarse graining. J. Chem. Theory Comput 7, 2981–2988. [PubMed: 26605486]

Berberian K, Torres AJ, Fang Q, Kisler K, and Lindau M (2009). F-actin and myosin II accelerate catecholamine release from chromaffin granules. J. Neurosci 29, 863–870. [PubMed: 19158310]

Berendsen HJC, Postma JPM, Vangunsteren WF, Dinola A, and Haak JR (1984). Molecular-dynamics with coupling to an external bath. J. Chem. Phys. 81, 3684–3690.

Borhani DW, Rogers DP, Engler JA, and Brouillette CG (1997). Crystal structure of truncated human apolipoprotein A-I suggests a lipid-bound conformation. Proc. Natl. Acad. Sci. U S A 94, 12291–12296. [PubMed: 9356442]

Breckenridge LJ, and Almers W (1987). Currents through the fusion pore that forms during exocytosis of a secretory vesicle. Nature 328, 814–817. [PubMed: 2442614]

Breckenridge WC, Gombos G, and Morgan IG (1972). The lipid composition of adult rat brain synaptosomal plasma membranes. Biochim. Biophys. Acta 266, 695–707. [PubMed: 4339171]

Bussi G, Donadio D, and Parrinello M (2007). Canonical sampling through velocity rescaling. J. Chem. Phys 126, 014101. [PubMed: 17212484]

Chang CW, Chiang CW, Gaffaney JD, Chapman ER, and Jackson MB (2016). Lipid-anchored synaptobrevin provides little or no support for exocytosis or liposome fusion. J. Biol. Chem 291, 2848–2857. [PubMed: 26663078]

Chow RH, von Rüden L, and Neher E (1992). Delay in vesicle fusion revealed by electrochemical monitoring of single secretory events in adrenal chromaffin cells. Nature 356, 60–63. [PubMed: 1538782]

Darden T, York D, and Pedersen L (1993). Particle mesh Ewald—an N.Log(N) method for Ewald sums in large systems. J. Chem. Phys 98, 10089–10092.

Dhara M, Yarzagaray A, Makke M, Schindeldecker B, Schwarz Y, Shaaban A, Sharma S, Böckmann RA, Lindau M, Mohrmann R, and Bruns D (2016). v-SNARE transmembrane domains function as catalysts for vesicle fusion. eLife 5, e17571. [PubMed: 27343350]

Estévez-Herrera J, Domínguez N, Pardo MR, González-Santana A, Westhead EW, Borges R, and Machado JD (2016). ATP: The crucial component of secretory vesicles. Proc. Natl. Acad. Sci. U S A 113, E4098–E4106. [PubMed: 27342860]

Fang Q, Berberian K, Gong LW, Hafez I, Sørensen JB, and Lindau M (2008). The role of the C terminus of the SNARE protein SNAP-25 in fusion pore opening and a model for fusion pore mechanics. Proc. Natl. Acad. Sci. U S A 105, 15388–15392. [PubMed: 18829435]

Gerhardt GA, and Adams RN (1982). Determination of diffusion coefficients by flow injection analysis. Anal. Chem 54, 2618–2620.

Goldman DE (1943). Potential, impedance, and rectification in membranes. J. Gen. Physiol 27, 37–60. [PubMed: 19873371]

Gong LW, Di Paolo G, Diaz E, Cestra G, Diaz ME, Lindau M, De Camilli P, and Toomre D (2005). Phosphatidylinositol phosphate kinase type I gamma regulates dynamics of large dense-core vesicle fusion. Proc. Natl. Acad. Sci. U S A 102, 5204–5209. [PubMed: 15793002]

Gong LW, de Toledo GA, and Lindau M (2007). Exocytotic catecholamine release is not associated with cation flux through channels in the vesicle membrane but Na^+ influx through the fusion pore. Nat. Cell Biol 9, 915–922. [PubMed: 17643118]

Gu RX, Ingólfsson HI, de Vries AH, Marrink SJ, and Tieleman DP (2017). Ganglioside-lipid and ganglioside-protein interactions revealed by coarse-grained and atomistic molecular dynamics simulations. J. Phys. Chem. B 121, 3262–3275. [PubMed: 27610460]

Haigh JR, Parris R, and Phillips JH (1989). Free concentrations of sodium, potassium and calcium in chromaffin granules. Biochem. J 259, 485–491. [PubMed: 2719661]

Hess B, Bekker H, Berendsen HJC, and Fraaije JGEM (1997). LINCS: a linear constraint solver for molecular simulations. J. Comput. Chem 18, 1463–1472.

Hess B, Kutzner C, van der Spoel D, and Lindahl E (2008). GROMACS 4: algorithms for highly efficient, load-balanced, and scalable molecular simulation. J. Chem. Theory Comput. 4, 435–447. [PubMed: 26620784]

Hille B (2001). Ion Channels of Excitable Membranes (Sunderland, MA: Sinauer Associates).

Huang M, Rathore SS, and Lindau M (2019). Drug testing complementary metal-oxide-semiconductor chip reveals drug modulation of transmitter release for potential therapeutic applications. J. Neurochem. 151, 38–49. [PubMed: 31274190]

Humphrey W, Dalke A, and Schulten K (1996). VMD: visual molecular dynamics. J. Mol. Graph. 14, 33–38, 27–28.

Kopell WN, and Westhead EW (1982). Osmotic pressures of solutions of ATP and catecholamines relating to storage in chromaffin granules. J. Biol. Chem. 257, 5707–5710. [PubMed: 6802820]

Kukol A (2009). Lipid models for united-atom molecular dynamics simulations of proteins. J. Chem. Theory Comput. 5, 615–626. [PubMed: 26610227]

Lindau M, and Gomperts BD (1991). Techniques and concepts in exocytosis: focus on mast cells. Biochim. Biophys. Acta 1071, 429–471. [PubMed: 1751542]

Lins RD, and Hünenberger PH (2005). A new GROMOS force field for hexopyranose-based carbohydrates. J. Comput. Chem. 26, 1400–1412. [PubMed: 16035088]

Marrink SJ, Risselada HJ, Yefimov S, Tieleman DP, and de Vries AH (2007). The MARTINI force field: coarse grained model for biomolecular simulations. J. Phys. Chem. B 111, 7812–7824. [PubMed: 17569554]

Monticelli L, Kandasamy SK, Periole X, Larson RG, Tieleman DP, and Marrink SJ (2008). The MARTINI coarse-grained force field: extension to proteins. J. Chem. Theory Comput. 4, 819–834. [PubMed: 26621095]

Mosharov EV, and Sulzer D (2005). Analysis of exocytotic events recorded by amperometry. Nat. Methods 2, 651–658. [PubMed: 16118635]

Ng B, and Barry PH (1995). The measurement of ionic conductivities and mobilities of certain less common organic ions needed for junction potential corrections in electrophysiology. J. Neurosci. Methods 56, 37–41. [PubMed: 7715244]

Ngatchou AN, Kisler K, Fang Q, Walter AM, Zhao Y, Bruns D, Sørensen JB, and Lindau M (2010). Role of the synaptobrevin C terminus in fusion pore formation. Proc. Natl. Acad. Sci. U S A 107, 18463–18468. [PubMed: 20937897]

Oostenbrink C, Villa A, Mark AE, and van Gunsteren WF (2004). A biomolecular force field based on the free enthalpy of hydration and solvation: the GROMOS force-field parameter sets 53A5 and 53A6. J. Comput. Chem. 25, 1656–1676. [PubMed: 15264259]

Parrinello M, and Rahman A (1981). Polymorphic transitions in single-crystals—a new molecular-dynamics method. J. Appl. Phys. 52, 7182–7190.

Parsons TD, Coorssen JR, Horstmann H, and Almers W (1995). Docked granules, the exocytic burst, and the need for ATP hydrolysis in endocrine cells. Neuron 15, 1085–1096. [PubMed: 7576652]

Pol-Fachin L, Rusu VH, Verli H, and Lins RD (2012). GROMOS 53A6GLYC, an Improved GROMOS Force Field for Hexopyranose-Based Carbohydrates. J. Chem. Theory Comput. 8, 4681–4690. [PubMed: 26605624]

Pollard HB, Shindo H, Creutz CE, Pazoles CJ, and Cohen JS (1979). Internal pH and state of ATP in adrenergic chromaffin granules determined by 31P nuclear magnetic resonance spectroscopy. J. Biol. Chem. 254, 1170–1177. [PubMed: 33185]

Scott WR, Hünenberger PH, Tironi IG, Mark AE, Billeter SR, Fennen J, Torda AE, Huber T, and Krüger P (1999). The GROMOS biomolecular simulation program package. J. Phys. Chem. A 103, 3596–3607.

Sharma S, and Lindau M (2018a). The fusion pore, 60 years after the first cartoon. FEBS Lett. 592, 3542–3562. [PubMed: 29904915]

Sharma S, and Lindau M (2018b). Molecular mechanism of fusion pore formation driven by the neuronal SNARE complex. Proc. Natl. Acad. Sci. U S A 115, 12751–12756. [PubMed: 30482862]

Sharma S, Kim BN, Stansfeld PJ, Sansom MS, and Lindau M (2015). A coarse grained model for a lipid membrane with physiological composition and leaflet asymmetry. PLoS ONE 10, e0144814. [PubMed: 26659855]

Shin W, Ge L, Arpino G, Villarreal SA, Hamid E, Liu H, Zhao WD, Wen PJ, Chiang HC, and Wu LG (2018). Visualization of membrane pore in live cells reveals a dynamic-pore theory governing fusion and endocytosis. Cell 173, 934–945.e12. [PubMed: 29606354]

Smart OS, Coates GM, Sansom MS, Alder GM, and Bashford CL (1998). Structure-based prediction of the conductance properties of ion channels. Faraday Discuss. 111, 185–199.

Stansfeld PJ, and Sansom MS (2011). From coarse grained to atomistic: a serial multiscale approach to membrane protein simulations. J. Chem. Theory Comput. 7, 1157–1166. [PubMed: 26606363]

Stein A, Weber G, Wahl MC, and Jahn R (2009). Helical extension of the neuronal SNARE complex into the membrane. Nature 460, 525–528. [PubMed: 19571812]

Takamori S, Holt M, Stenius K, Lemke EA, Grønborg M, Riedel D, Urlaub H, Schenck S, Brügger B, Ringler P, et al. (2006). Molecular anatomy of a trafficking organelle. Cell 127, 831–846. [PubMed: 17110340]

Van Der Spoel D, Lindahl E, Hess B, Groenhof G, Mark AE, and Berendsen HJ (2005). GROMACS: fast, flexible, and free. J. Comput. Chem. 26, 1701–1718. [PubMed: 16211538]

Wightman RM, Jankowski JA, Kennedy RT, Kawagoe KT, Schroeder TJ, Leszczyszyn DJ, Near JA, Diliberto EJ Jr., and Viveros OH (1991). Temporally resolved catecholamine spikes correspond to single vesicle release from individual chromaffin cells. Proc. Natl. Acad. Sci. U S A 88, 10754–10758. [PubMed: 1961743]

Zhao Y, Fang Q, Herbst AD, Berberian KN, Almers W, and Lindau M (2013). Rapid structural change in synaptosomal-associated protein 25 (SNAP25) precedes the fusion of single vesicles with the plasma membrane in live chromaffin cells. Proc. Natl. Acad. Sci. U S A 110, 14249–14254. [PubMed: 23940346]

Highlights

- Exocytotic transmitter release is an electrodiffusion process
- Narrow fusion pores are cation selective
- Fusion pore ion selectivity decreases as the fusion pore expands

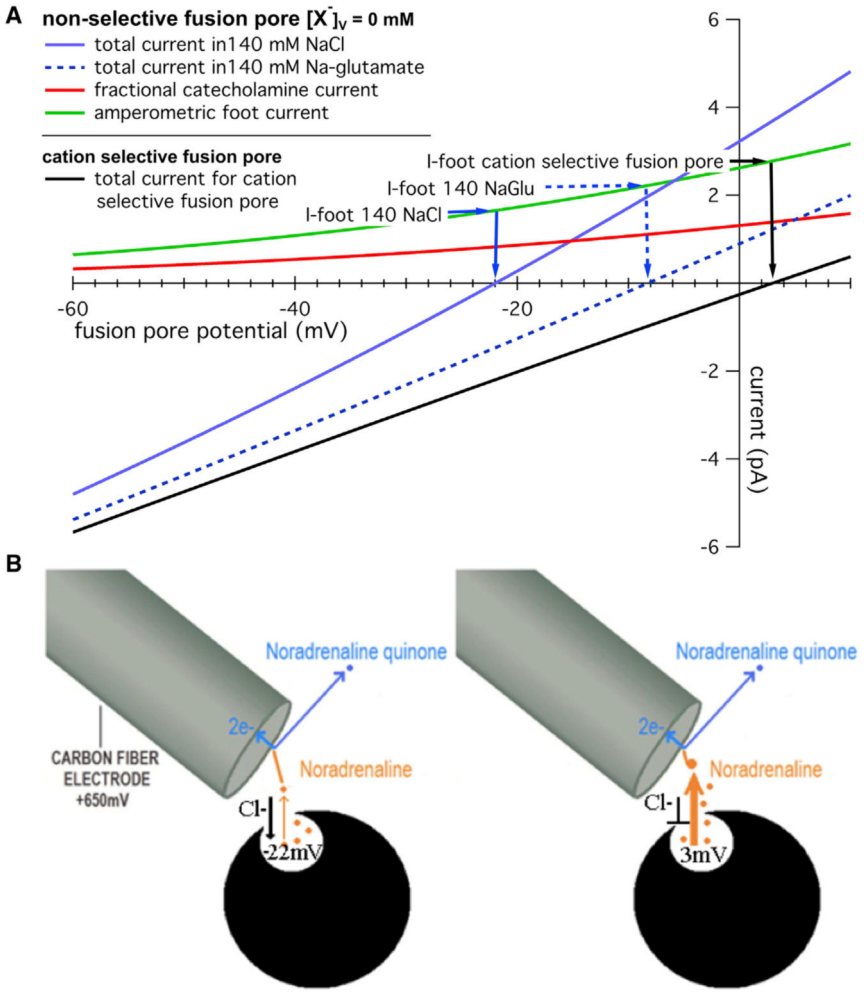

Figure 1. Ion selectivity of the fusion pore affects its zero current potential, catecholamine flux, and I_{foot}

(A) Nernst-Planck electrodiffusion calculations using Equation 3. Current-voltage relations calculated for an anion-permeable fusion pore for Cl^--based solution (solid blue line) and Glu^--based bath solution (dashed blue line) and for a cation-selective fusion pore (black line). Zero current potentials are indicated by vertical arrows. The amperometric current (green line) is twice the fractional CA^+ current (red line) because two electrons are transferred per detected monovalent CA^+ molecule.

(B) Schematic illustrating that for a nonselective fusion pore, which anions can permeate, the negative zero current potential reduces efflux of catecholamines compared with a cation-selective fusion pore (right panel), where regardless of the anion present in the solution, anions will not permeate the fusion pore, and efflux of catecholamines is increased because of the more positive intravesicular potential.

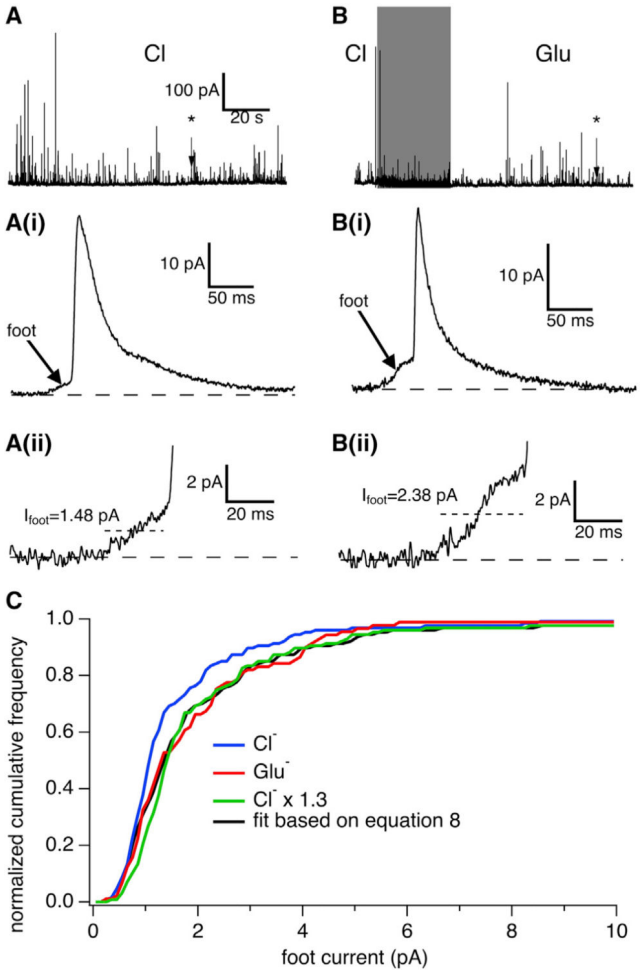

Figure 2. Comparison of I_{foot} in Cl^-- and Glu^--based solutions measured in an individual cell stimulated by intracellular application of 10 μM free Ca^2 using a whole-cell patch pipette

(A and B) Amperometric recordings obtained in Cl^--based solution (A) and Glu^--based solution (B). The gray bar indicates the time during which the solution was changed. Amperometric spikes during this period were excluded from the analysis. Individual amperometric spikes indicated by an asterisk are shown on expanded scale in Ai and Bi and the respective foot currents further expanded in Aii and Bii, respectively.

(C) Cumulative frequency distributions of I_{foot} in Cl^- solution (blue) and Glu^- solution (red). The black dashed line is the fitted curve transforming the blue curve on the basis of Equation 8. The green curve shows the cumulative distribution that is obtained when the foot current values measured in Cl^- are multiplied by a factor of 1.3, as expected for an anion-permeable fusion pore.

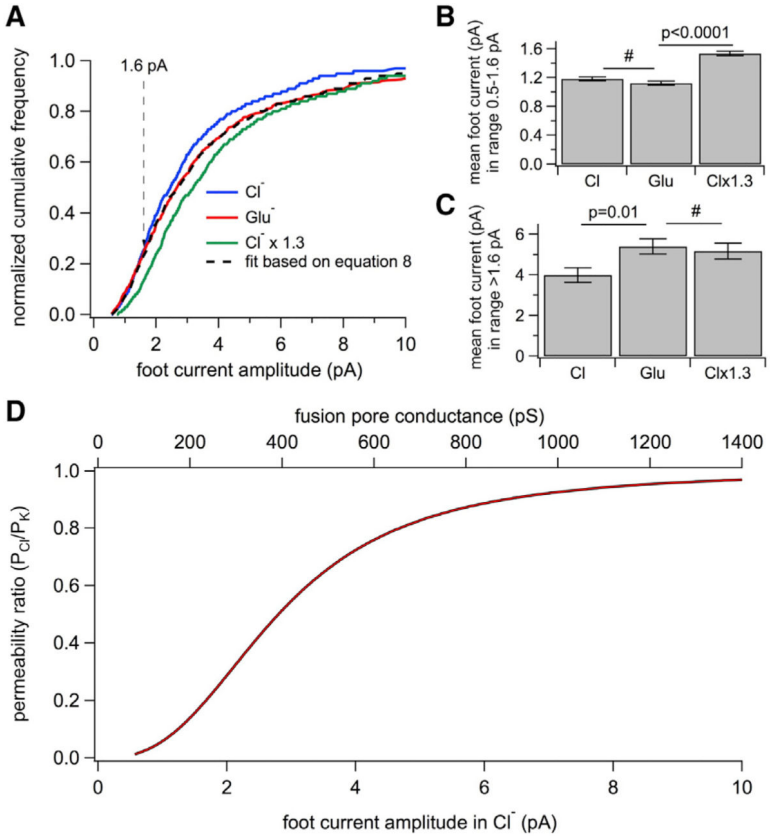

Figure 3. Comparison of I_{foot} in Cl^-- and Glu^--based solutions measured with ionomycin stimulation

(A) Cumulative distribution of I_{foot} in Cl^--based (blue line), and Glu^--based (red line) solutions. For comparison, the curve for Cl^- is scaled to 30% larger foot current values, stretching the Cl^- curve by a factor of 1.3 along the abscissa (green line), as expected for an anion-permeable fusion pore when Cl^- is replaced by D-glutamate$^-$. The black dashed curve is the fitted curve transforming the blue curve on the basis of Equation 8.

(B and C) Mean foot currents in Cl^- solution and Glu^- solution in the range 0.5–1.6 pA (B) and >1.6 pA (C). The bar labeled Clx1.3 shows the value obtained when the foot current values measured in Cl^- are multiplied by a factor of 1.3, corresponding to the green curve in (A). Statistical data are expressed as mean ± SEM and p values for test of significance were determined through least square regression in JMP software as described in STAR Methods section “Quantification and statistical analysis.”

(D) Gradual change in anion permeability as a function of foot current (bottom scale) and fusion pore conductance (top scale).

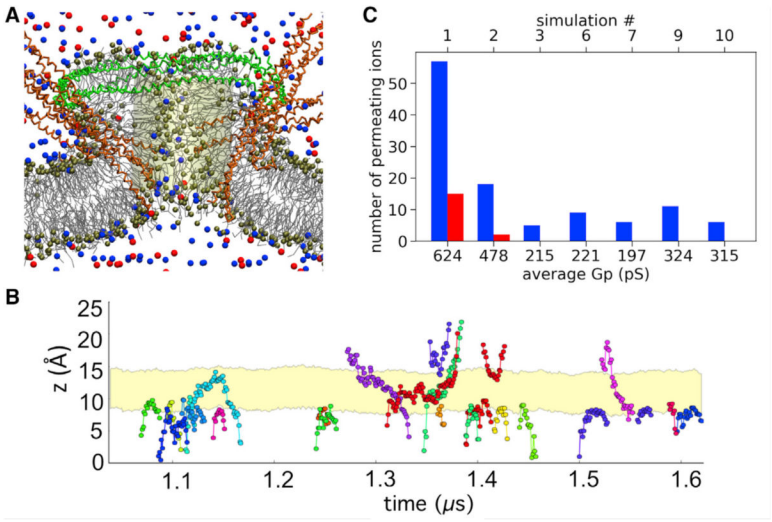

Figure 4. Ion permeation through a fusion pore traversing a nanodisc and a planar membrane in CGMD simulation

(A) Snapshot of fusion pore with surrounding cations (blue), anions (red), SNARE proteins (orange), and MSP nanodisc scaffold protein (green).

(B) Selected trajectories of anions attempting to permeate the fusion pore from Sim 1. In most cases they do not pass the narrow center of the pore (shaded yellow in A and B).

(C) Number of fusion pore permeations of cations (blue) and anions (red) from individual simulations (top axis). Average uncorrected fusion pore conductances are given in bottom axis.

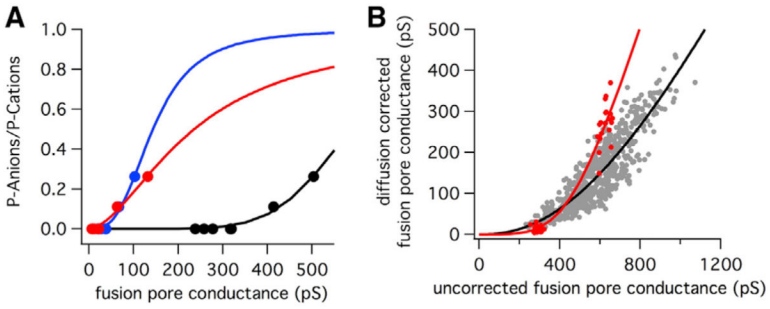

Figure 5. Anion/cation permeability ratio increases with fusion pore conductance in molecular dynamics simulations

(A) Permeability ratios as a function of uncorrected structure-based fusion pore conductance (black symbols) and as a function of diffusion-corrected conductance on the basis of coarse-grained (blue symbols) and atomistic (red symbols) simulations. Continuous lines are fits with Equation 4.

(B) Correction of structure-based fusion pore conductance for reduced water self-diffusion. Conductance values (5 ns averages) from all CGMD trajectory segments with open fusion pore and lifetime >25 ns (gray dots) and from the last 19 ns of two 25-ns-long atomistic simulations (1 ns averages) (red dots). Lines are corresponding fits using Equation 11.

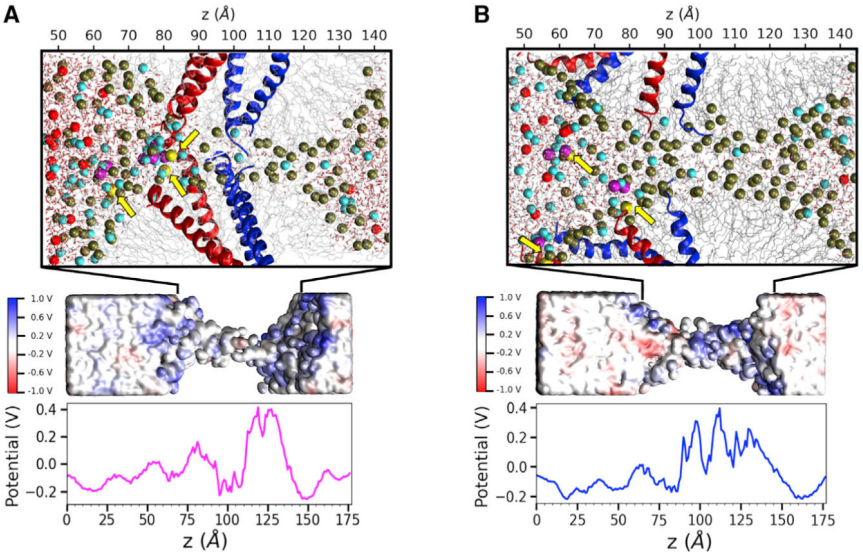

Figure 6. Electrostatic potential inside two fusion pores with different conductance in the presence of ions from a single snapshot of the simulation trajectory

Fusion pores had diffusion-corrected conductance of 13 pS (A) and 292 pS (B), respectively. The middle panels show the fusion pores in a surface representation, colored according to the electrostatic potential at each grid point of the mesh. The top panels show zoomed-in views of the fusion pores. The SNARE proteins are represented as ribbons (Syb2, blue; Stx1, red). The phosphates of the lipid headgroups are shown as brown spheres. Each pore has three PIP2 lipids. The phosphorous atoms of the phosphodiester linkage are shown as yellow spheres (and marked with arrows), while each of phosphorus atoms of the two inositol-PO4 groups are shown as magenta spheres. The waters in the pore are shown as thick lines (oxygen in red and hydrogen in white), and the lipids are represented as gray lines. The bottom panel shows the calculated potential inside the pore along the z axis.

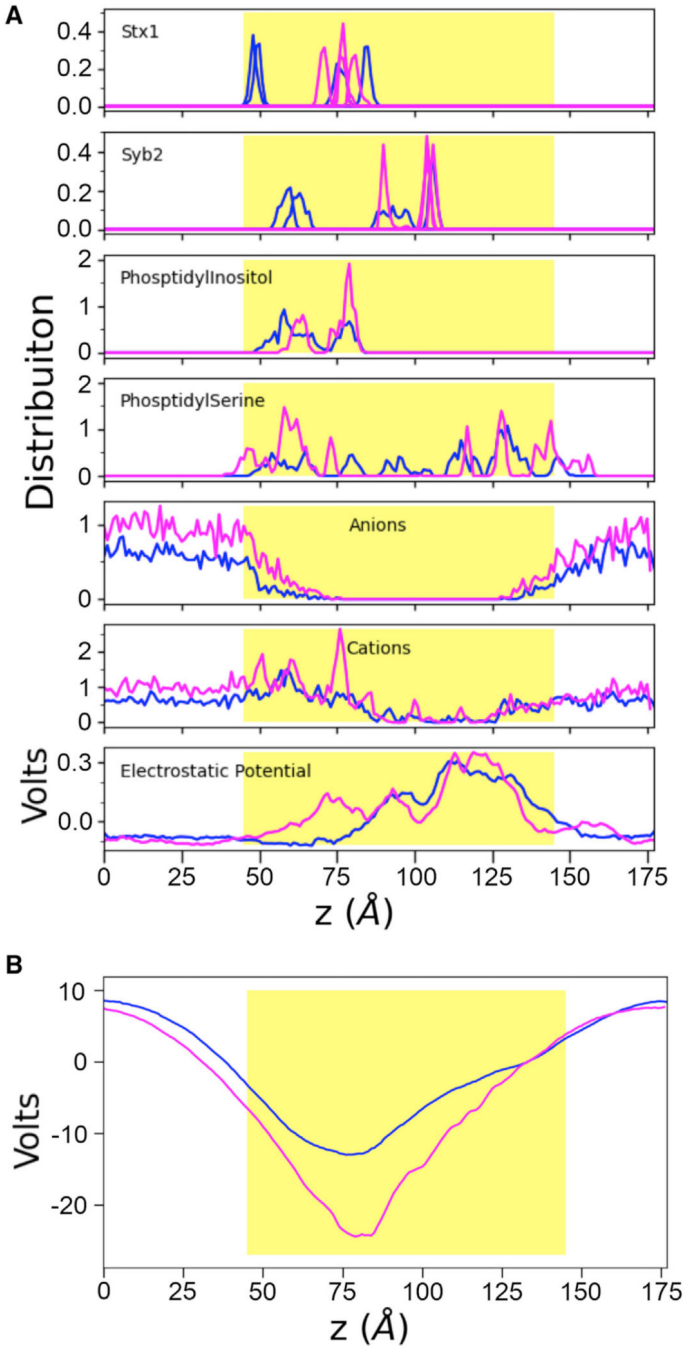

Figure 7. Charge distributions and electrostatic potential in the low-conductance (red) and high-conductance (blue) fusion pore averaged over 10 ns

The yellow box indicates the location of the fusion pore region shown in the top panels of Figure 6.

(A) Distributions of charges and electrostatic potential in the fusion pore. From top to bottom: the locations of the carbon atoms of Stx1 and Syb2 C-termini, the three atoms of PIP2 (one from the phosphodiester linkage and the two from the inositol-PO_4 groups), the two atoms of PS lipids (a phosphorous atom and a carboxyl atom), the cations, the anions, and the mean electrostatic potential are shown.

(B) The mean electrostatic potential in the pore excluding the charges from cations and anions.

KEY RESOURCES TABLE

REAGENT or RESOURCE	SOURCE	IDENTIFIER
Biological samples		
Healthy bovine chromaffin primary cell line culture	Owasco Meat Co Inc.	N/A
Chemicals, peptides, and recombinant proteins		
$NaH_2PO_4.H_2O$	Mallinckrodt Chemicals	CHEBI: 37585, cat no.: 7892
D-Glutamic Acid	Sigma-Aldrich	cat no.: G1001
L-Glutamine	GIBCO	CHEBI: 18050, cat no.: 25030–081
Pen-Strep	GIBCO	CHEBI: 102135, cat no.: 15750–060
MEM vitamins	GIBCO	cat no.: 11120–052
MEM amino acids	GIBCO	cat no.: 11140–050
0.1% Bovine Serum Albumin Fraction V	Sigma-Aldrich	cat no.: A7906
0.02% poly-D-lysine	Sigma-Aldrich	cat no.: P7280
Ionomycin calcium salt	Sigma-Aldrich	cat no.: I0634
MgATP	Sigma-Aldrich	cat no.: A9187
Software and algorithms		
GROMACS v. 4.6.5	Van Der Spoel et al., 2005	http://www.gromacs.org/Downloads_of_outdated_releases
53A6 force field	Oostenbrink et al., 2004.	https://onlinelibrary.wiley.com/doi/10.1002/jcc.20090
MARTINI force field	Marrink et al., 2007	http://cgmartini.nl/index.php/force-field-parameters
Visual Molecular Dynamics (VMD) v. 1.9.3	Humphrey et al., 1996.	https://www.ks.uiuc.edu/Development/Download/download.cgi?PackageName=VMD
PMEPot Plugin v. 1.0	Aksimentiev and Schulten, 2005	https://www.ks.uiuc.edu/Research/vmd/plugins/pmepot/
Fragment-based protocol (CG2AT)	Stansfeld and Sansom, 2011	https://bitbucket.org/claughton/cecam-setup/wiki/MemProtMD%20Pipeline
IGOR Pro 8	WaveMetrics, Inc.	https://www.wavemetrics.com/downloads/current
Quanta Analysis 8.20, IGOR Procedure File	Mosharov and Sulzer, 2005	https://cumc.columbia.edu/dept/neurology/sulzer/download.html
JMP Pro	SAS Institute	https://it.cornell.edu/softwarelicensing/jmp-licensing
Other		
Borosilicate glass capillary	Hilgenberg GmbH, Germany	1.8 mm o.d.
Carbon fiber 5 μm diameter	Amoco Performance Products, Inc.	Thornel T650/42 6K